Helmholtz-Zentrum Dresden-Rossendorf (HZDR)

HELMHOLTZ ZENTRUM
DRESDEN ROSSENDORF

Symmetries and localization properties of defect modes in metamaterial magnonic superlattices

Gallardo, R. A.; Schneider, T.; Roldán-Molina, A.; Langer, M.; Núñez, A. S.; Lenz, K.; Lindner, J.; Landeros, P.;

Originally published:

May 2018

Physical Review B 97(2018), 174404

DOI: https://doi.org/10.1103/PhysRevB.97.174404

Perma-Link to Publication Repository of HZDR:

https://www.hzdr.de/publications/Publ-26634

Release of the secondary publication
on the basis of the German Copyright Law § 38 Section 4.

Symmetries and localization properties of defect modes in metamaterial magnonic superlattices

R. A. Gallardo,[1] T. Schneider,[2,3] A. Roldán-Molina,[4] M. Langer,[2,5] A. S. Núñez,[6] K. Lenz,[2] J. Lindner,[2] and P. Landeros[1]

[1] *Departamento de Física, Universidad Técnica Federico Santa María, Avenida España 1680, Valparaíso, Chile*
[2] *Institute of Ion Beam Physics and Materials Research, Helmholtz-Zentrum Dresden-Rossendorf e.V., P.O. Box 510119, 01314 Dresden, Germany*
[3] *Department of Physics, Technische Universität Chemnitz, Reichenhainer Str. 70, 09126 Chemnitz, Germany*
[4] *Universidad de Aysén, Ovispo Vielmo 62, Coyhaique, Chile*
[5] *Paul Scherrer Institut, 5232 Villigen PSI, Switzerland*
[6] *Departamento de Física, Facultad de Ciencias Físicas y Matemáticas, Universidad de Chile, Casilla 487-3, 8370415 Santiago, Chile*

(Dated: November 10, 2017)

Symmetries and localization properties of defect modes of a one-dimensionsional bi-component magnonic superlattice are theoretically studied. The magnonic superlattice can be seen as a periodic array of nanostripes, where stripes with different width, termed as defect stripes, are periodically introduced. By controlling the geometry of the defect stripes, a transition from dispersive to practically flat spin-wave defect modes can be observed inside the magnonic band gaps. It is shown that the spin-wave profile of the defect modes can be either symmetric or asymmetric by depending on the geometry of the defect. Due to the localization peculiarities of the defect modes, a particular magnonic superlattice is proposed, wherein the excitation of either symmetric or antisymmetric flat modes is enabled at the same time. Also, it is demonstrated that the relative frequency position of the asymmetric mode inside the band gap does not significantly change with the application of an external field, while the symmetric modes move to the edges of the frequency band gaps. The results are complemented by numerical simulations, where an excellent agreement is observed between both methods. The proposed theory allows exploring different ways to control the dynamic properties of the defect modes in metamaterial magnonic superlattices, which can be useful for applications on multifunctional microwave devices operating over a broad frequency range.

I. INTRODUCTION

The dynamic properties of spin waves (SWs) in magnonic devices with artificial periodic modulation of the magnetic or geometrical parameters have been a glowing research area in the last years.[1–9] The magnetic metameterials termed magnonic crystals (MCs) have been widely studied since its excitation spectrum present magnonic band gaps (BGs), which can be controlled by external magnetic fields.[10–12] These systems can be created by artificial modulation of the magnetic properties,[13–16] or by modification of the film geometry.[17–26] The magnonic BGs are strongly dependent of the geometrical parameters of the periodic lattice, whose spatial range usually lies in the hundreds of nanometers. Around these gaps, SWs can be excited in well defined allowed frequency bands, where, depending on the wave vector, the waves may have a standing or a propagating character. In particular, the standing SWs are localized at the borders of the Brillouin zones of the periodic structure and therefore, such waves can be only excited at some specific wave vectors. This characteristic makes difficult to channelize or guide the spin waves along specific regions, which turns out key for applications in magnonic waveguides[9,12] and tunable narrow passband SW filters.[27,28]

In the field of photonic crystals, it is well known that the incorporation of a local defect breaks the translational symmetry and electromagnetic modes can appear within the forbidden band gaps.[29–32] For instance, the addition of extra dielectric material in one of the unit cells gives rise to modes within the BGs that behaves like a donor atom in a semiconductor, while the removal of dielectric material from the crystal produces acceptor-like modes.[29] This extra degree of freedom allows manipulating and controlling the properties of light in dielectric metamaterials. Indeed, the defect-induced phenomena in photonic crystals have been applied for controlling the spontaneous light emission,[33–35] and trapping optical pulses.[36] In analogy to photonic crystals, it has been also demonstrated that the controlled introduction of periodic defects in magnonic crystals induces defect modes (DMs) inside de BGs that can beneficially enrich the SW band structure of the magnetic metamaterial.[27,28] Here, the periodic lattice induces translational symmetry on the SWs that can be broken with the controlled introduction of periodic defects, that is, a change in the periodic structure that redefines the unit cell, in the same way that in a crystal with a complex unit cell. This system can be seen as a *magnonic superlattice* (MSL), which consists of a periodic array of magnonic supercells.

The emergence of DMs lying into the band gaps has been predicted[37–39] and recently observed experimentally in magnonic superlattices.[27,28] Multilayered ferromag-

netic structures having variations in the magnetization, uniaxial anisotropy and/or thicknesses have been theoretically studied in backward volume (BV) geometry in Refs. 37–39. A theoretical analysis of short-wavelength perturbations in two-dimensional MCs with point defects was performed by Yang, Yun and Cao,[40–43] where different configurations of the point defects were investigated. Defect-induced phenomena in one dimensional bi-component MC with structural defects were more recently investigated by Brillouin light scattering (BLS) measurements and by numerical simulations.[27,28] Here, arrays of 250 nm-width Py stripes were fabricated in such a way that every ten wires, there is a defect wire having a width ranging from 300 to 500 nm. Regarding to these BLS measurements, a direct comparison between theory and experiment has not been feasible so far, maybe because magnetostatic terms were neglected in previous theoretical works. Since the recent experiments were realized in the Damon-Eshbach (DE) geometry at small wave vectors (around 10 μm^{-1}), the dynamic dipolar contribution must be taken into account. Furthermore, the analysis of an arbitrary angle of the magnetization respect to the symmetry axes of the crystal has not been reported so far and also, there is not a model that considers a general way to introduce arbitrary arrays of periodic defects on the MC. Besides, the evolution of the DMs as a function of the external field has not been deeply explored. These aspects clearly do not allow a deeper study of the dynamic properties on MSL structures.

In this paper, symmetries and localization properties of defect modes on one-dimensional bi-component magnonic superlattices are theoretically addressed and contrasted with micromagnetic simulations. It is shown that by controlling the lattice parameter of the defect stripes, a transition from slight to almost null dispersion of the defect modes is observed. Besides, by changing the width of the defect stripes the symmetry nature as well as the frequency of the DMs can be modified. It is also demonstrated that the external field can change the relative position of the symmetric modes respect to the BG, while the antisymmetric ones remain in the same relative frequency position. The possibility of exciting both symmetric and antisymmetric DMs at the same time is also proposed.

II. THEORETICAL DESCRIPTION

By combining a defect-free lattice with a periodic array of stripes with different width, a one-dimensional bi-component magnonic superlattice is formed, as shown in Fig. 1. Here, the lattice parameter of the defect-free crystal is a, while the lattice parameter of the defect stripes is νa. Here, $\nu = 1, 2, 3...$, is introduced to locate a defective wire each ν repetitions, allowing for a general description of the MSL.

The dynamics of the magnetic system is described

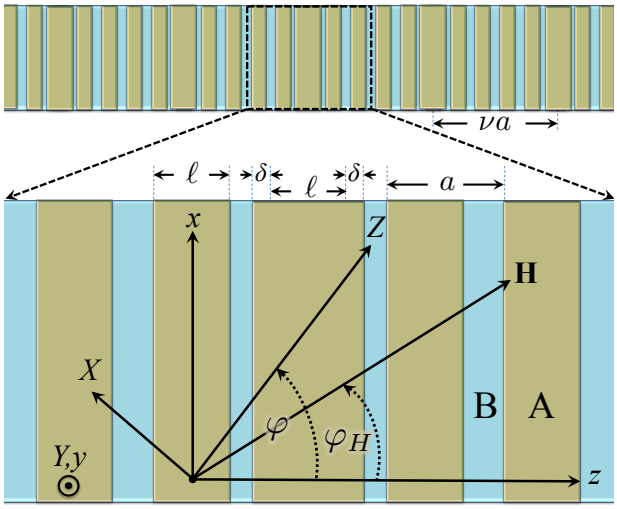

FIG. 1. Geometry of the one-dimensional bi-component magnonic superlattice, which is composed of materials A and B. The lattice parameter of the periodic array of nanostripes is a, while νa corresponds to the lattice parameter of the defect stripes. Note that ν represents the number of lattice repetitions that are necessary to form the MSL. The width of nanostripes (defects) is ℓ ($\ell + 2\delta$). The SWs are assumed to propagate in z-direction, while the equilibrium magnetization (external field) makes an angle φ ($\varphi_{\rm h}$) with the z-axis. The zoom denotes the unit cell of the superlattice structure.

by the Landau-Lifshitz (LL) equation $\dot{\mathbf{M}}(\mathbf{r};t) = -\gamma \mathbf{M}(\mathbf{r};t) \times \mathbf{H}^{\rm e}(\mathbf{r};t)$, where γ is the absolute value of the gyromagnetic ratio, $\mathbf{M}(\mathbf{r};t)$ is the magnetization and $\mathbf{H}^{\rm e}(\mathbf{r};t)$ is the effective field. For small magnetization deviations around the equilibrium state, both magnetization and effective field can be written as $\mathbf{M}(\mathbf{r};t) = M_{\rm s}(\mathbf{r})\hat{Z} + \mathbf{m}(\mathbf{r};t)$ and $\mathbf{H}^{\rm e}(\mathbf{r};t) = \mathbf{H}^{\rm e0}(\mathbf{r}) + \mathbf{h}^{\rm e}(\mathbf{r};t)$, respectively. Here, $M_{\rm s}(\mathbf{r})$ is the saturation magnetization, $\hat{Z}$ represents the equilibrium orientation of the magnetization and $\mathbf{m}(\mathbf{r};t) = m_X(\mathbf{r};t)\hat{X} + m_Y(\mathbf{r};t)\hat{Y}$ corresponds to the dynamic magnetization. Besides, $\mathbf{H}^{\rm e0}(\mathbf{r})$ is the static part of the effective field and $\mathbf{h}^{\rm e}(\mathbf{r};t)$ is the time-dependent part. Now, assuming harmonic time dependence, $\mathbf{m}(\mathbf{r};t) = \mathbf{m}(\mathbf{r})e^{i\omega t}$, and neglecting the second order terms in $\mathbf{m}(\mathbf{r})$, the LL dynamic equation can be written as

$$i(\omega/\gamma)m_X(\mathbf{r}) = -m_Y(\mathbf{r})H_Z^{\rm e0}(\mathbf{r}) + M_{\rm s}(\mathbf{r})h_Y^{\rm e}(\mathbf{r}) \qquad (1)$$

and

$$i(\omega/\gamma)m_Y(\mathbf{r}) = m_X(\mathbf{r})H_Z^{\rm e0}(\mathbf{r}) - M_{\rm s}(\mathbf{r})h_X^{\rm e}(\mathbf{r}); \qquad (2)$$

with ω being the angular frequency. Note that in Eqs. (1) and (2), the equilibrium conditions $M_{\rm s}(\mathbf{r})H_Y^{\rm e0}(\mathbf{r}) = 0$ and $M_{\rm s}(\mathbf{r})H_X^{\rm e0}(\mathbf{r}) = 0$ have been considered. Now, the effective field is given by $\mathbf{H}^{\rm e}(\mathbf{r}) = \mathbf{H} + \mathbf{H}^{\rm ex}(\mathbf{r}) + \mathbf{H}^{\rm d}(\mathbf{r})$, where $\mathbf{H}$ is the external field, $\mathbf{H}^{\rm ex}(\mathbf{r})$ is the exchange field and $\mathbf{H}^{\rm d}(\mathbf{r})$ is the dipolar field. These fields are detailed in appendix A. According to Bloch's theorem, the dynamic

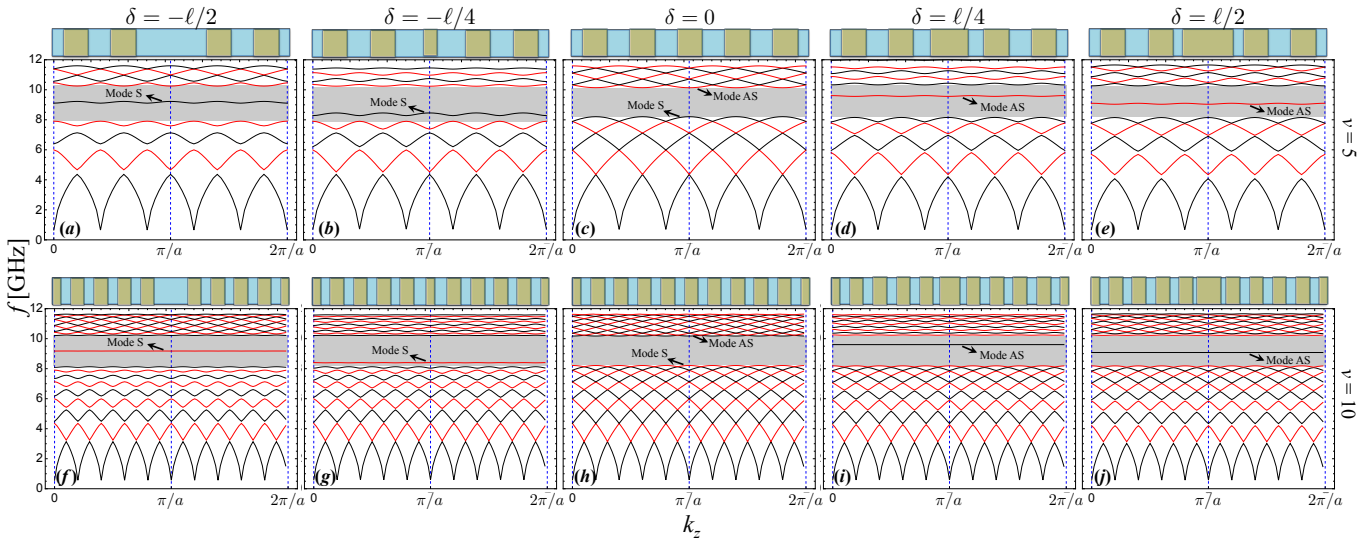

FIG. 2. In (a)–(e) the dispersion of a supercell composed by $\nu = 5$ is shown, while in (f)–(j) the case $\nu = 10$ is depicted. The parameter δ has been varied from $-\ell/2$ up to $\ell/2$ in such a way that the width $(\ell + 2\delta)$ of the SL ranges from 0 to a. The upper inset on each plot schematically illustrates the unit cell of the magnonic superlattice structure.

magnetization components are expanded into Fourier series as $\mathbf{m}(\mathbf{r}) = \sum_{\mathbf{G}} \mathbf{m}(\mathbf{G}) e^{i(\mathbf{G}+\mathbf{k})\cdot\mathbf{r}}$, where $\mathbf{G} = G_n^\nu \hat{z}$ denotes the reciprocal lattice vector. Here $G_n^\nu = (2\pi/\nu a)n$, where n, and ν are integer numbers. The saturation magnetization and exchange length are respectively given by $M_\mathrm{s}(\mathbf{r}) = \sum_{\mathbf{G}} M_\mathrm{s}(\mathbf{G}) e^{\mathbf{G}\cdot\mathbf{r}}$ and $\lambda_\mathrm{ex}(\mathbf{r}) = \sum_{\mathbf{G}} \lambda_\mathrm{ex}(\mathbf{G}) e^{\mathbf{G}\cdot\mathbf{r}}$. Now, by including the effective fields in Eqs. (1) and (2), the following eigenvalue problem is obtained:

$$\tilde{\mathbf{A}}\ \mathbf{m}_\mathbf{G} = i\frac{\omega}{\gamma}\ \mathbf{m}_\mathbf{G} \tag{3}$$

where $\mathbf{m}_\mathbf{G}^\mathrm{T} = [m_X(G_1), ..., m_X(G_N), m_Y(G_1), ..., m_Y(G_N)]$ is the eigenvector and $\tilde{\mathbf{A}}$ is given by

$$\tilde{\mathbf{A}} = \begin{pmatrix} \tilde{\mathbf{A}}^{XX} & \tilde{\mathbf{A}}^{XY} \\ \tilde{\mathbf{A}}^{YX} & \tilde{\mathbf{A}}^{YY} \end{pmatrix}. \tag{4}$$

By using standard numerical methods and a convergence test to check the reliability of the results, the eigenvalues and eigenvectors of Eq. (3) can be obtained. The matrix elements are given in appendix A.

III. MICROMAGNETIC SIMULATIONS

Micromagnetic simulations were performed with the GPU-accelerated open-source code MuMax^3.[44] The bi-component magnonic crystal was modeled as a 100 μm x 20 nm x 30 nm stripe. Periodic boundary conditions were applied to regain the thin film nature of the system. The stripe was discretized into 16384 x 4 x 1 cells, which results in a cell size of 6.1 nm x 5 nm x 30 nm. The material parameters in the simulation were chosen as mentioned below. In addition, the Gilbert damping value of 0.01 was chosen. Two kind of simulation were performed for the magnonic supercell. At first the SW dispersion relation was calculated with a sinc-pulse in time and space.[45] In addition to the approach in Ref. 45, the sinc-pulse was shifted in space by $5(L_z/N_z)$ in respect to the unit cell to also excite the total antisymmetric SW modes. The resulting SW dispersion relations were obtained by performing a 2D Fast-Fourier-Transform (FFT) for every lines for cells in the z-direction. Furthermore, the ferromagnetic resonance (FMR) response of the system has been simulated. Therefore, the time evolution of the system excited with a sinc-pulse in time was recorded.[46] To also excite the antisymmetric SW mode an additional linear offset was added. The SW frequencies were extracted as the summation of the spatial FFT in time of each cell.

IV. RESULTS AND DISCUSSION

To study dynamic properties of the system, standard values of Cobalt and Permalloy are employed.[27] Namely, the magnetic properties of the material B are taken from the Cobalt and they are: $M_\mathrm{s}^\mathrm{B} = 1100$ kA/m and $A_\mathrm{ex}^\mathrm{B} = 2.5 \cdot 10^{-11}$ J/m. On the other side, magnetic properties of the material A are linked to the Permalloy ($Ni_{80}Fe_{20}$), i.e. $M_\mathrm{s}^\mathrm{A} = 730$ kA/m and $A_\mathrm{ex}^\mathrm{A} = 1.1 \cdot 10^{-11}$ J/m. Here, A_ex is exchange constant and hence $\lambda_\mathrm{ex} = \sqrt{2A_\mathrm{ex}/4\pi M_\mathrm{s}^2}$. For both materials, an effective gyromagnetic ratio of $\gamma = 0.0185556$ GHz/G and thickness $d = 30$ nm are used. Also, the lattice parameter of the defect-free crystal is $a = 500$ nm and its width is $\ell = 250$ nm. At 200 reciprocal lattice vectors, a convergence of the numerical solutions of Eq. (3) is reached.

Fig. 2 shows the SW dispersion of a MSL composed by $\nu = 5$ $[(a)$–$(e)]$ and $\nu = 10$ $[(f)$–$(j)]$ in the Damon-

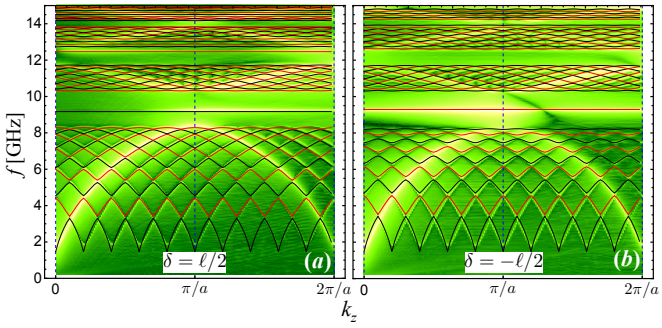

FIG. 3. Figures (a) and (b) show the dispersion relation of the SWs calculated for $\delta = \ell/2$ and $\delta = -\ell/2$, respectively; and $\nu = 10$. The lines correspond to the theoretical calculations, while he color code represents the numerical simulations, where the brighter color indicates a maximum of the response.

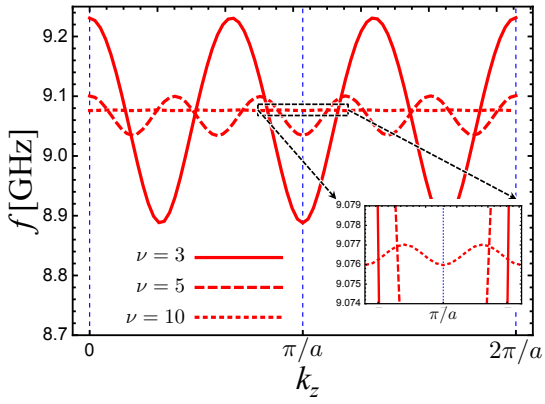

FIG. 4. Defect mode AS evaluated at $\delta = \ell/2$ for $\nu = 3$, 5 and 10. The inset shows the zoom of the dispersion around the Brillouin zone ($k_z = \pi/a$), where a dispersion with small oscillation amplitude is observed even at $\nu = 10$.

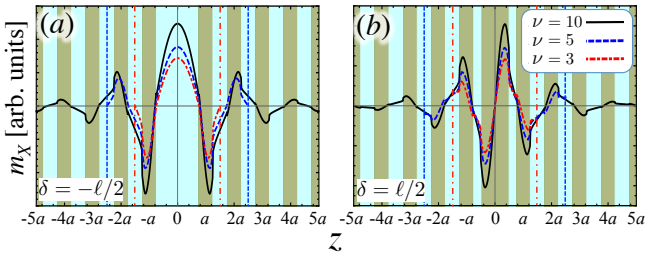

FIG. 5. Defect mode for different values of ν. In (a) the case $\delta = -\ell/2$ is depicted, where the SW excitation exhibits a symmetric profile around the modified stripes, while in (b) an antisymmetric SW profile is observed for $\delta = \ell/2$. The vertical dashed (dotted-dashed) line depicts the unit cell for $\nu = 5$ ($\nu = 3$).

Eshbach geometry at $H = 0$. Here, the equilibrium magnetization is given by $\varphi = \pi/2$ and the SW propagation is along the z-axis. The parameter δ has been varied from $-\ell/2$ up to $\ell/2$ in such a way that the width $(\ell+2\delta)$ goes from 0 to a. In both cases, $\nu = 5$ and $\nu = 10$, a nearly flat defect mode labeled as AS (S) moves from the high (low) frequency region into the BG when $\delta > 0$ ($\delta < 0$). If $\delta < 0$, the mode located at the low-frequency edge of the BG (mode S) enters into the magnonic BG and it is localized near to the center of the gap at $\delta = -\ell/2$. On the other side, at $\delta > 0$ the mode located at the high-frequency edge of the BG gets into the BG and also is located around the center of the gap at $\delta = \ell/2$. Once both modes S and AS are inside the band gap they are characterized for a nearly flat dispersion. The label S (AS) is due to the symmetric (antisymmetric) SW profile of the mode (see the discussion of Fig. 5). Overall, one can see that at higher values of ν the dispersion of the modes become flatter. Note that the case shown in Fig. 2(f) is coincident with the system measured in Ref. 27, in deed all the parameters used in this paper are the same. Therefore, by comparing Fig. 3(b) of Ref. 27 with Fig. 2(f), one can see an excellent agreement between them.

Fig. 3 shows a comparison between the micromagnetic simulations and theoretical results for a wider range of frequencies. Here, the dispersion relation of the SWs is calculated for a superlattice characterized by $\nu = 10$, while $\delta = \ell/2$ in Fig. 3(a), and $\delta = -\ell/2$ in Fig. 3(b). The lines correspond to the theoretical calculations, while the color code represents the numerical simulations, where the brighter color indicates a maximum of the response. Overall, an excellent agreement is reach between both methods, which corroborates the theoretical approach. Since a larger range of frequencies is plotted, one can see that DMs are present in the first two BGs for the case $\delta = \ell/2$, while in the case $\delta = -\ell/2$ just one mode is located in the first band gap. On the other side, it is possible to see that the defect modes always have a periodic dispersion with finite oscillation amplitude, nonetheless this amplitude dramatically decreases as the lattice parameter of the MSL νa increases. This is depicted in Fig. 4, where the cases $\nu = 3$, 5 and 10 are shown. One can observe that the position of the DMs is not significantly affected by ν, nevertheless the oscillation amplitude and the number of peaks are clearly dependent on ν. Thus, at $\nu = 10$ for instance the mode inside the BG seem to have no dispersion, which is in concordance with recent BLS experiments and micromagnetic simulations.[27,28]

The spatial spin-wave profiles obtained from the in-plane dynamic component m_X are depicted in Fig. 5 for $\delta = \pm\ell/2$ and $\nu = 3$, 5 and 10. The vertical dotted-dashed (dashed) line depicts the unit cell for $\nu = 3$ ($\nu = 5$). The main conclusions of these calculations are that the defect modes correspond to SW excitations mainly localized in the modified stripes of width $\ell + 2\delta$, and they can be symmetric or antisymmetric depending on the sign of δ. For instance, if $\delta < 0$ the mode is symmetric as shown Fig. 5(a), while it becomes antisymmetric when $\delta > 0$ [see Fig. 5(b)]. These symmetry properties can be reversed if the materials A and B are

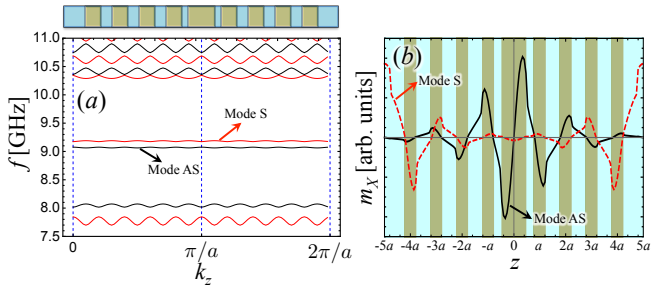

FIG. 6. In (a) a superlattice structure with $\nu = 10$, $\delta = \ell/2$ and $\delta' = -\ell/2$ is depicted, while (b) shows the dynamic magnetization component m_X of both S and AS modes.

exchanged (not shown). On the other hand, from Fig. 5 it is easy to see that the amplitude of the defect modes decreases quickly as z increases and this effect becomes enhanced as ν increases. Thus, for $\nu = 10$, the amplitude of the SW excitation becomes almost zero at $z = \pm 5a$. This localization of the defect mode allows implementing the following: If the width of the fifth stripe (localized at $z = \pm\ 5a$) in the lattice with $\nu = 10$ is geometrically modified, both the frequency and localization of the defect mode should not change notoriously, since the area around $z = \pm\ 5a$ is irrelevant for the dynamics of both S or AS modes. To corroborate this behavior, one can take the case $\nu = 10$ with $\delta > 0$, in such a way to excite the AS mode, and at the same time modify the width of the fifth stripe by changing $\ell \to \ell + 2\delta'$ (with $\delta' < 0$), in order to excite both S and AS modes inside the magnonic band gap at the same time. The calculation of a superlattice with two alternating widths $\ell + 2\delta$ and $\ell + 2\delta'$ every five stripes can be implemented in the theory by replacing the term $\cos(n\pi)\sin(n\pi\ell/10a)$ in Eq. (B3) by $\cos(n\pi)\sin[n\pi(\ell + 2\delta')/10a]$, in such a way that δ modifies the width of the stripe located at $z = j_s 10a$ and δ' modifies the width of the stripe in $z = (j_s{+}1/2)10a$, with $j_s = 0, 1, 2, 3....$ In Fig. 6 such a superlattice structure with two different defects characterized by $\delta = \ell/2$ and $\delta' = -\ell/2$ is shown. As was previously established, both the frequency and localization of S and AS modes are not modified notoriously [see Figs. 2(f) and 2(j)]. The interesting feature of this kind of system is that clearly uncoupled symmetric and antisymmetric defect modes are excited at the same time, which respectively evolves from the upper and lower boundaries of the band gap, as δ and δ' are incremented in magnitude.

In Fig. 7(a) the evolution of the S and AS modes for a MSL with two different defects is shown as a function of the magnitude of δ and δ'. Here, it is assumed that $\delta > 0$ and $\delta' < 0$. Figs. 7(b)–(c) show the simulated and calculated dispersions for some specific values of δ and $|\delta'|$. Note that there is a crossing point near to $\delta = |\delta'| = 115$ nm, where both S and AS modes have the same frequency. Then, for the case $\delta = |\delta'| = 125$ nm, the S mode have a slightly larger frequency than the AS mode, as opposed for the cases where $\delta = |\delta'| < 115$ nm.

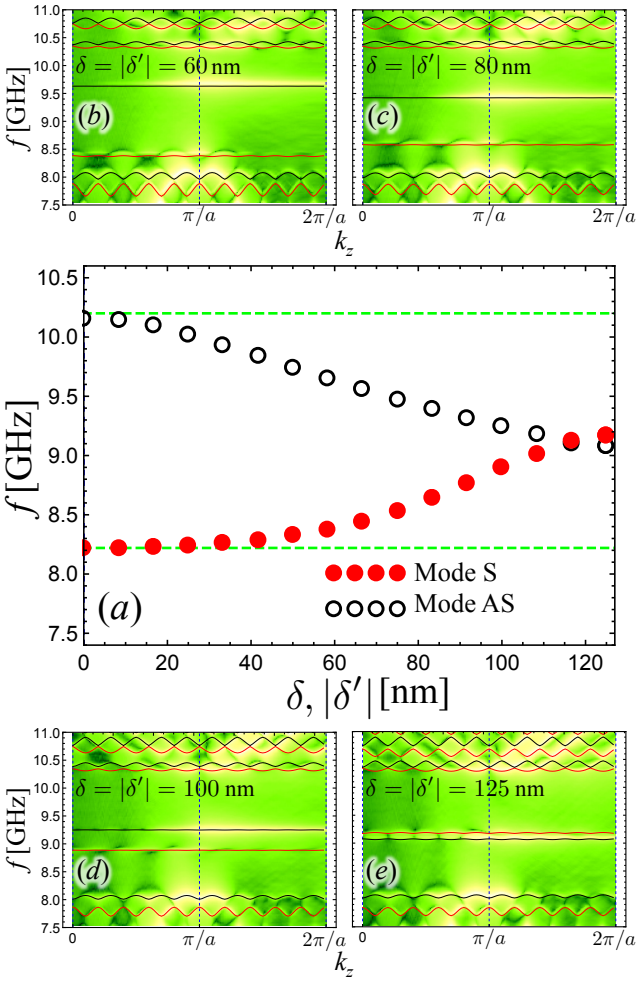

FIG. 7. a) Symmetric and antisymmetric modes as a function of δ and the magnitude of δ', since $\delta' < 0$. Figures (b)-(e) depict the simulated and theoretically calculated SW dispersion for some values of δ and $|\delta'|$.

The symmetry features of the defect modes should be useful, for instance, in FMR experiments, since the nature of the external excitation in typical FMR setups allows to excite only the symmetric modes, and therefore under specific conditions the S mode should be detected at $k_z = 0$. The applied field dependence of the S and AS modes is shown in Fig. 8(a) at the FMR limit ($k_z = 0$). Here, the low-frequency mode is plotted together with the S and AS modes, where one can appreciate that the symmetric mode is clearly influenced by the field, in such a way that at higher values of H the mode moves towards the high-frequency edge of the band gap (gray zone). Nevertheless, the AS mode remains almost in the same relative frequency position respect to the BG. Figs. 8(b) and (c) show the SW profile for the AS and S modes, respectively. Clearly, the profile of the AS modes remains constant as the external field increases, while the S mode is notably modified. Since the dynamic part of the Zeeman energy density can be

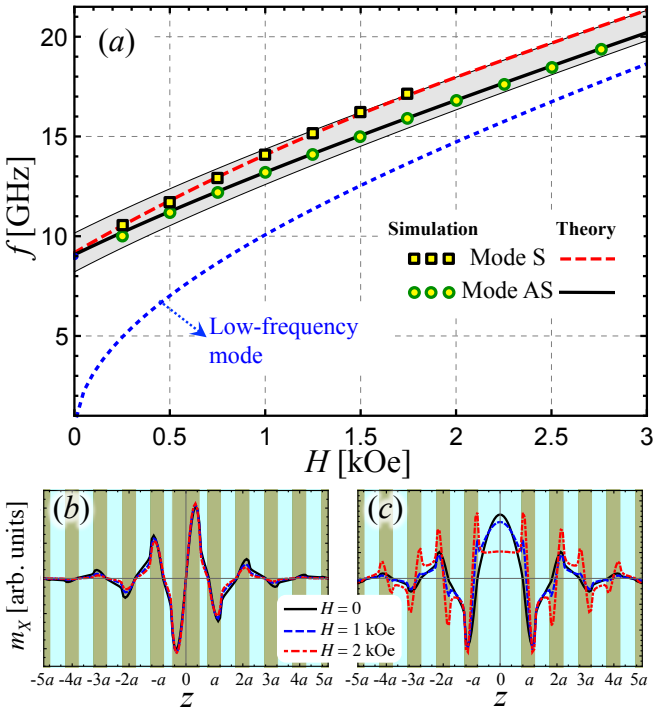

FIG. 8. (a) Evolution of the symmetric (dashed line) and antisymmetric (solid line) modes as a function of the external field for $k_z = 0$. Here, the S mode is excited with $\delta = -\ell/2$, and the AS mode with $\delta = \ell/2$. The gray zone depicts the BG width and the (blue) dotted line indicate the low-frequency FMR mode. In (b) and (c) the SW profiles are depicted for the AS and S mode, respectively, where it is clearly seen that only the S mode in influenced by the field.

expressed as $\epsilon_Z = -(H/2M_s)(m_X^2 + m_Y^2)$, it is expected that the AS modes do not have an additional dynamic contribution in ϵ_Z, since the term $m_X^2 + m_Y^2$ is not modified. Nevertheless, since for the S mode m_X changes with the field, then the relative frequency position of the symmetric mode is influenced by the field. Therefore, it is demonstrated that the symmetric modes have a limited range of field where they can be observed, since when these modes reach the borders of the BG they are extended along the crystal and therefore they can not be externally detected.[27] On the other side, once the antisymmetric mode is excited, it should be observed in a wider range of fields.

V. FINAL REMARKS

Dynamic characteristics of one-dimensional bi-component magnonic superlattices have been theoretically studied by taking into account both dipolar and exchange interactions. Symmetries, localization as well as field-dependent properties of the nearly flat defect modes have been theoretically addressed and contrasted with micromagnetic simulations. It is found that by controlling the width of the modified stripe of the magnonic superlattice either symmetric or antisymmetric modes can be excited. Also, by modifying the separation between defects, a transition from dispersive to practically flat spin-wave branches is observed inside the magnonic band gaps. Due to the localization features of the defect modes, a system is proposed that consists of a superlattice with wide and narrow stripe-like defects, where it is possible to observe uncoupled symmetric and antisymmetric modes at the same time. It is also demonstrated that the symmetric modes have a limited range of field where they can be observed, while the antisymmetric ones should be externally detected in a wider range of external fields. The dynamic properties observed in this work can be used to engineer the band structures of magnonic superlattice systems, since the controlled introduction of defects provides additional degrees of freedom, which can be of fundamental importance for technological applications in magnonic crystal based devices.

ACKNOWLEDGMENTS

RAG acknowledges financial support from CONICYT PAI/ACADEMIA, under contract 79140033. This work was supported by CONICYT, FONDECYT 1161403 and Basal Program for Centers of Excellence, Grant FB0807 CEDENNA, CONICYT.

Appendix A: Effective fields and matrix elements

For the periodic structure shown in Fig. 1, the static exchange field is given by

$$H_Z^{\mathrm{ex0}}(\mathbf{r}) = -4\pi \sum_{\mathbf{G},\mathbf{G}'} \mathbf{G}\cdot(\mathbf{G}'+\mathbf{G}) M_s(\mathbf{G})[\lambda_{\mathrm{ex}}(\mathbf{G}')]^2 \times e^{i(\mathbf{G}'+\mathbf{G})\cdot\mathbf{r}}, \tag{A1}$$

where the other two static components are zero ($H_X^{\mathrm{ex0}} = H_Y^{\mathrm{ex0}} = 0$). On the other side, the dynamic exchange components are

$$h_{X,Y}^{\mathrm{ex}}(\mathbf{r}) = -4\pi \sum_{\mathbf{G},\mathbf{G}'} (\mathbf{G}+\mathbf{k})\cdot(\mathbf{G}'+\mathbf{G}+\mathbf{k})[\lambda_{\mathrm{ex}}(\mathbf{G}')]^2 \times m_{X,Y}(\mathbf{G}) e^{i(\mathbf{G}'+\mathbf{G}+\mathbf{k})\cdot\mathbf{r}}. \tag{A2}$$

According to Fig. 1 the external applied field is $H_Z^0 = H\cos(\varphi_h - \varphi)$ and $H_X^0 = H\sin(\varphi_h - \varphi)$, where φ_h (φ) is the angle between the external field (equilibrium magnetization) and the z-axis. On the other hand, the dynamic components of the dipolar field are

$$h_Y^{\mathrm{d}}(\mathbf{r}) = -\sum_{\mathbf{G}} m_Y(\mathbf{G})\zeta(\mathbf{G},\mathbf{k}) e^{i(\mathbf{G}+\mathbf{k})\cdot\mathbf{r}} \tag{A3}$$

and

$$h_X^{\rm d}(\mathbf{r}) = 4\pi \sum_{\mathbf{G}} m_X(\mathbf{G})\xi(\mathbf{G})^2[\frac{\zeta(\mathbf{G},\mathbf{k})-1}{|\mathbf{G}+\mathbf{k}|^2}]e^{i(\mathbf{G}+\mathbf{k})\cdot\mathbf{r}}. \tag{A4}$$

Here, it has been defined $\xi(\mathbf{G}) = (G_n^\nu + k_z)\sin\psi$ and

$$\zeta(\mathbf{G},\mathbf{k}) = \frac{2\sinh[|\mathbf{G}+\mathbf{k}|d/2]e^{-|\mathbf{G}+\mathbf{k}|d/2}}{|\mathbf{G}+\mathbf{k}|d}. \tag{A5}$$

Also, the Z-component of the static dipolar field is

$$H_Z^{\rm d0}(\mathbf{r}) = -4\pi \sum_{\mathbf{G}} M_{\rm s}(\mathbf{G})\chi(\mathbf{G})^2 \frac{1-\zeta(\mathbf{G},0)}{|\mathbf{G}|^2} e^{i\mathbf{G}\cdot\mathbf{r}}, \tag{A6}$$

where $\chi(\mathbf{G}) = G_n^\nu \cos\varphi$.

By introducing the effective fields in the dynamic equation of motion, the submatrices in Eq. (4) are given by

$$\mathbf{A}^{XX}_{\mathbf{G},\mathbf{G}'} = \mathbf{A}^{YY}_{\mathbf{G},\mathbf{G}'} = 0, \tag{A7a}$$

$$\mathbf{A}^{XY}_{\mathbf{G},\mathbf{G}'} = -H\cos(\varphi-\varphi_{\rm h})\delta_{\mathbf{G},\mathbf{G}'} + 4\pi M_{\rm s}(\mathbf{G}-\mathbf{G}')\left[\chi(\mathbf{G}-\mathbf{G}')^2\frac{1-\zeta(\mathbf{G}-\mathbf{G}',0)}{|\mathbf{G}-\mathbf{G}'|^2} - \zeta(\mathbf{G}',\mathbf{k})\right]$$
$$- 4\pi\sum_{\mathbf{G}''} M_{\rm s}(\mathbf{G}-\mathbf{G}'')\left[(\mathbf{G}'+\mathbf{k})\cdot(\mathbf{G}''+\mathbf{k}) - (\mathbf{G}-\mathbf{G}'')\cdot(\mathbf{G}-\mathbf{G}')\right][\lambda_{\rm ex}(\mathbf{G}''-\mathbf{G}')]^2 \tag{A7b}$$

$$\mathbf{A}^{YX}_{\mathbf{G},\mathbf{G}'} = H\cos(\varphi-\varphi_{\rm h})\delta_{\mathbf{G},\mathbf{G}'} - 4\pi M_{\rm s}(\mathbf{G}-\mathbf{G}')\left[\chi(\mathbf{G}-\mathbf{G}')^2\frac{1-\zeta(\mathbf{G}-\mathbf{G}',0)}{|\mathbf{G}-\mathbf{G}'|^2} + \xi(\mathbf{G}')^2[\frac{\zeta(\mathbf{G}',\mathbf{k})-1}{|\mathbf{G}'+\mathbf{k}|^2}])\right]$$
$$+ 4\pi\sum_{\mathbf{G}''} M_{\rm s}(\mathbf{G}-\mathbf{G}'')\left[(\mathbf{G}'+\mathbf{k})\cdot(\mathbf{G}''+\mathbf{k}) - (\mathbf{G}-\mathbf{G}'')\cdot(\mathbf{G}-\mathbf{G}')\right][\lambda_{\rm ex}(\mathbf{G}''-\mathbf{G}')]^2. \tag{A7c}$$

Appendix B: Fourier coefficient of one-dimensional magnonic superlattices

For a general one-dimensional superlattice, the Fourier coefficient of the saturation magnetization can be obtained by analyzing the one-dimensional periodic structure. Thus, according to Fig. 1, it is straightforward to see that

$$M_{\rm s}(G_n^\nu) = \frac{1}{2\nu a}\left[M_{\rm s}^{\rm A}\int_{-\frac{\nu a}{2}}^{-\frac{\nu a-\ell}{2}} e^{-iG_n^\nu z}dz + M_{\rm s}^{\rm B}\int_{-\frac{\nu a-\ell}{2}}^{-\frac{(\nu-2)a+\ell}{2}} e^{-iG_n^\nu z}dz + M_{\rm s}^{\rm A}\int_{-\frac{(\nu-2)a+\ell}{2}}^{-\frac{(\nu-2)a-\ell}{2}} e^{-iG_n^\nu z}dz\right.$$
$$\left. + ... + M_{\rm s}^{\rm A}\int_{-\frac{\ell+2\delta}{2}}^{\frac{w+2\delta}{2}} e^{-iG_n^\nu z}dz + ... + M_{\rm s}^{\rm B}\int_{\frac{(\nu-2)a+\ell}{2}}^{\frac{\nu a-\ell}{2}} e^{-iG_n^\nu z}dz + M_{\rm s}^{\rm A}\int_{\frac{\nu a-\ell}{2}}^{\frac{\nu a}{2}} e^{-iG_n^\nu z}dz\right], \tag{B1}$$

if ν is an even number (2, 4, 6...). On the other side, if ν is an odd number (1, 3, 5...), the coefficient is calculated as

$$M_{\rm s}(G_n^\nu) = \frac{1}{2\nu a}\left[M_{\rm s}^{\rm B}\int_{-\frac{\nu a}{2}}^{-\frac{(\nu-1)a+\ell}{2}} e^{-iG_n^\nu z}dz + M_{\rm s}^{\rm A}\int_{-\frac{(\nu-1)a+\ell}{2}}^{-\frac{(\nu-1)a-\ell}{2}} e^{-iG_n^\nu z}dz + M_{\rm s}^{\rm B}\int_{-\frac{(\nu-1)a-\ell}{2}}^{-\frac{(\nu-3)a+\ell}{2}} e^{-iG_n^\nu z}dz\right.$$
$$\left. + ... + M_{\rm s}^{\rm A}\int_{-\frac{\ell+2\delta}{2}}^{\frac{\ell+2\delta}{2}} e^{-iG_n^\nu z}dz + ... + M_{\rm s}^{\rm A}\int_{\frac{(\nu-1)a-\ell}{2}}^{\frac{(\nu-1)a+\ell}{2}} e^{-iG_n^\nu z}dz + M_{\rm s}^{\rm B}\int_{\frac{(\nu-1)a+\ell}{2}}^{\frac{\nu a}{2}} e^{-iG_n^\nu z}dz\right]. \tag{B2}$$

By carrying out the appropriate integration of Eqs. (B1) and (B2), the result can be generalized as

$$M_{\rm s}(G_n^\nu) = M_{\rm s}^{\rm B}\frac{\sin(n\pi)}{n\pi} + \frac{M_{\rm s}^{\rm A}-M_{\rm s}^{\rm B}}{n\pi}\left\{\sin\left[\frac{n\pi(\ell+2\delta)}{\nu a}\right] + \Psi(n,\nu)\sin\left(\frac{n\pi\ell}{\nu a}\right)\right\}, \tag{B3}$$

where

$$\Psi(n,\nu) = \cos(n\pi)\cos^2\left(\nu\frac{\pi}{2}\right) - 2 + 2\sum_{j=1}^{\nu}\left\{\cos\left[\frac{(j-1)n\pi}{\nu}\right]\cos^2\left[(j+1)\frac{\pi}{2}\right]\cos^2\left[(\nu+1)\frac{\pi}{2}\right] + \cos\left[\frac{(j-2)n\pi}{\nu}\right]\cos^2\left(j\frac{\pi}{2}\right)\cos^2\left(\nu\frac{\pi}{2}\right)\right\}. \quad \text{(B4)}$$

Here, ν represents the number of lattice repetitions that are necessary to form the MSL. A similar structure can be used for the exchange length $\lambda_{\rm ex}(G_n^\nu)$. Therefore, by choosing δ and ν any 1D bi-component magnonic superlattice can be modeled.

[1] J. O. Vasseur, L. Dobrzynski, B. Djafari-Rouhani, and H. Puszkarski, Phys. Rev. B **54**, 1043 (1996).
[2] S. Neusser, B. Botters, and D. Grundler, Phys. Rev. B **78**, 054406 (2008).
[3] S. Tacchi, F. Montoncello, M. Madami, G. Gubbiotti, G. Carlotti, L. Giovannini, R. Zivieri, F. Nizzoli, S. Jain, A. O. Adeyeye, and N. Singh, Phys. Rev. Lett. **107**, 127204 (2011).
[4] S. Tacchi, G. Duerr, J. W. Klos, M. Madami, S. Neusser, G. Gubbiotti, G. Carlotti, M. Krawczyk, and D. Grundler, Phys. Rev. Lett. **109**, 137202 (2012).
[5] Z. K. Wang, V. L. Zhang, H. S. Lim, S. C. Ng, M. H. Kuok, S. Jain, and A. O. Adeyeye, Appl. Phys. Lett. **94**, 083112 (2009).
[6] Z. K. Wang, V. L. Zhang, H. S. Lim, S. C. Ng, M. H. Kuok, S. Jain, and A. O. Adeyeye, ACS Nano **4**, 643 (2010).
[7] A. V. Chumak, V. I. Vasyuchka, A. A. Serga, M. P. Kostylev, V. S. Tiberkevich, and B. Hillebrands, Phys. Rev. Lett. **108**, 257207 (2012).
[8] H. Yu, G. Duerr, R. Huber, M. Bahr, T. Schwarze, F. Brandl, and D. Grundler, Nat. Commun. **4**, 2702 (2013).
[9] M. Krawczyk and D. Grundler, J. Phys.: Condens. Matter **26**, 123202 (2014).
[10] A. A. Serga, A. V. Chumak, and B. Hillebrands, J. Phys. D: Appl. Phys. **43**, 264002 (2010).
[11] V. V. Kruglyak, S. O. Demokritov, and D. Grundler, J. Phys. D: Appl. Phys. **43**, 264001 (2010).
[12] B. Lenk, H. Ulrichs, F. Garbs, and M. Münzenberg, Phys. Rep. **507**, 107 (2011).
[13] V. Kruglyak and R. Hicken, J. Magn. Magn. Mater. **306**, 191 (2006).
[14] I. Barsukov, F. M. Römer, R. Meckenstock, K. Lenz, J. Lindner, S. Hemken to Krax, A. Banholzer, M. Körner, J. Grebing, J. Fassbender, and M. Farle, Phys. Rev. B **84**, 140410 (2011).
[15] B. Obry, P. Pirro, T. Brächer, A. V. Chumak, J. Osten, F. Ciubotaru, A. A. Serga, J. Fassbender, and B. Hillebrands, Appl. Phys. Lett. **102**, 202403 (2013).
[16] R. A. Gallardo, A. Banholzer, K. Wagner, M. Körner, K. Lenz, M. Farle, J. Lindner, J. Fassbender, and P. Landeros, New J. Phys. **16**, 023015 (2014).
[17] A. V. Chumak, P. Pirro, A. A. Serga, M. P. Kostylev, R. L. Stamps, H. Schultheiss, K. Vogt, S. J. Hermsdoerfer, B. Laegel, P. A. Beck, and B. Hillebrands, Appl. Phys. Lett. **95**, 262508 (2009).
[18] K.-S. Lee, D.-S. Han, and S.-K. Kim, Phys. Rev. Lett. **102**, 127202 (2009).
[19] J. Ding, M. Kostylev, and A. O. Adeyeye, Phys. Rev. B **84**, 054425 (2011).
[20] P. Landeros and D. L. Mills, Phys. Rev. B **85**, 054424 (2012).
[21] F. Ciubotaru, A. V. Chumak, N. Y. Grigoryeva, A. A. Serga, and B. Hillebrands, J. Phys. D: Appl. Phys. **45**, 255002 (2012).
[22] J. W. Kłos, D. Kumar, J. Romero-Vivas, H. Fangohr, M. Franchin, M. Krawczyk, and A. Barman, Phys. Rev. B **86**, 184433 (2012).
[23] M. Krawczyk, S. Mamica, M. Mruczkiewicz, J. W. Klos, S. Tacchi, M. Madami, G. Gubbiotti, G. Duerr, and D. Grundler, J. Phys. D: Appl. Phys. **46**, 495003 (2013).
[24] M. Körner, K. Lenz, R. A. Gallardo, M. Fritzsche, A. Mücklich, S. Facsko, J. Lindner, P. Landeros, and J. Fassbender, Phys. Rev. B **88**, 054405 (2013).
[25] G. Gubbiotti, M. Kostylev, S. Tacchi, M. Madami, G. Carlotti, J. Ding, A. O. Adeyeye, F. Zighem, A. A. Stashkevich, E. Ivanov, and S. Samarin, J. Phys. D: Appl. Phys. **47**, 105003 (2014).
[26] M. Langer, F. Röder, R. A. Gallardo, T. Schneider, S. Stienen, C. Gatel, R. Hübner, L. Bischoff, K. Lenz, J. Lindner, P. Landeros, and J. Fassbender, Phys. Rev. B **95**, 184405 (2017).
[27] K. Di, V. L. Zhang, M. H. Kuok, H. S. Lim, S. C. Ng, K. Narayanapillai, and H. Yang, Phys. Rev. B **90**, 060405 (2014).
[28] V. L. Zhang, H. S. Lim, S. C. Ng, M. H. Kuok, X. Zhou, and A. O. Adeyeye, AIP Adv. **6**, 115106 (2016).
[29] E. Yablonovitch, T. J. Gmitter, R. D. Meade, A. M. Rappe, K. D. Brommer, and J. D. Joannopoulos, Phys. Rev. Lett. **67**, 3380 (1991).
[30] J. D. Joannopoulos, P. R. Villeneuve, and S. Fan, Nature **386**, 143 (1997).
[31] M. Bayindir, B. Temelkuran, and E. Ozbay, Phys. Rev. Lett. **84**, 2140 (2000).
[32] P. V. Braun, S. A. Rinne, and F. García-Santamaría, Adv. Mat. **18**, 2665 (2006).
[33] S. Ogawa, M. Imada, S. Yoshimoto, M. Okano, and S. Noda, Science **305**, 227 (2004).
[34] D. Englund, D. Fattal, E. Waks, G. Solomon, B. Zhang, T. Nakaoka, Y. Arakawa, Y. Yamamoto, and J. Vučković, Phys. Rev. Lett. **95**, 013904 (2005).
[35] T. S. Kao, T. T. Wu, C. W. Tsao, J. H. Lin, D. W. Lin,

S. J. Huang, T. C. Lu, H. C. Kuo, S. C. Wang, and Y. K. Su, IEEE J. Q. Elec. **52**, 1 (2016).
[36] A. H. Safavi-Naeini, J. T. Hill, S. Meenehan, J. Chan, S. Gröblacher, and O. Painter, Phys. Rev. Lett. **112**, 153603 (2014).
[37] S. Nikitov, P. Tailhades, and C. Tsai, J. Magn. Magn. Mater. **236**, 320 (2001).
[38] A. Kuchko, M. Sokolovskii, and V. Kruglyak, Phys. B: Cond. Matt. **370**, 73 (2005).
[39] V. V. Kruglyak, M. L. Sokolovskii, V. S. Tkachenko, and A. N. Kuchko, J. Appl. Phys. **99**, 08C906 (2006).
[40] H. Yang, G. Yun, and Y. Cao, J. Appl. Phys. **111**, 013908 (2012).
[41] H. Yang, G. Yun, and Y. Cao, J. Appl. Phys. **112**, 103911 (2012).
[42] H. Yang, G. Yun, and Y. Cao, J. Magn. Magn. Mater. **356**, 32 (2014).
[43] D. Xing, H. Yang, and Y. Cao, J. Magn. Magn. Mater. **377**, 286 (2015).
[44] A. Vansteenkiste, J. Leliaert, M. Dvornik, M. Helsen, F. Garcia-Sanchez, and B. Van Waeyenberge, AIP Adv. **4**, 107133 (2014).
[45] G. Venkat, D. Kumar, M. Franchin, O. Dmytriiev, M. Mruczkiewicz, H. Fangohr, A. Barman, M. Krawczyk, and A. Prabhakar, IEEE Trans. Mag. **49**, 524 (2013).
[46] R. D. McMichael and M. D. Stiles, J. Appl. Phys. **97**, 10J901 (2005).